AGU PUBLICATIONS

JGR

Journal of Geophysical Research: Solid Earth

RESEARCH ARTICLE
10.1002/2014JB011816

Key Points:
- Rate of contact overgrowth exceeds "frictional" contact growth
- Overgrowths are driven by surface curvature gradients
- Quartz asperities are not wetted at hydrothermal conditions

Correspondence to:
N. M. Beeler,
nbeeler@usgs.gov

Citation:
Beeler, N. M., and S. H. Hickman (2015), Direct measurement of asperity contact growth in quartz at hydrothermal conditions, *J. Geophys. Res. Solid Earth*, *120*, 3599–3616, doi:10.1002/2014JB011816.

Received 8 DEC 2014
Accepted 10 DEC 2014
Accepted article online 19 JAN 2015
Published online 5 MAY 2015

Direct measurement of asperity contact growth in quartz at hydrothermal conditions

N. M. Beeler[1] and Stephen H. Hickman[2]

[1]U.S. Geological Survey, Vancouver, Washington, USA, [2]U.S. Geological Survey, Menlo Park, California, USA

Abstract Earthquake recurrence requires interseismic fault restrengthening which results from solid-state deformation in room temperature friction and indentation experiments. In contrast, exhumed fault zones show solution-transport processes such as pressure solution, and contact overgrowths influence fault zone properties. In the absence of fluid flow, overgrowths are driven by gradients in surface curvature where material is dissolved, diffuses, and precipitates at the contact without convergence normal to the contact. To determine the rate of overgrowth for quartz, we conducted single-contact experiments in an externally heated pressure vessel. Convergence was continuously monitored using reflected light interferometry through a long-working-distance microscope. Contact normal force was constant with an initial effective normal stress of 1.7 MPa, temperature was between 350 and 530°C, and water pressure was constant at 150 MPa. Two control experiments were conducted: one dry at 425°C and one bimaterial (sapphire) at 425°C and 150 MPa water pressure. No contact growth or convergence was observed in the controls. For wet single-phase contacts, growth was initially rapid and then decreased with time. No convergence was observed. Fluid inclusions indicate that the contact is not uniformly wetted. The contact is bounded by small regions of high aperture, reflecting local free-face dissolution as the source for the overgrowth. The apparent activation energy is ~125 kJ/mol. Extrapolation predicts rates of contact area increase orders of magnitude faster than in dry, room temperature and hydrothermal friction experiments, suggesting that natural strength recovery near the base of the seismogenic zone could be dominated by contact overgrowth.

1. Introduction

For an earthquake to recur following stress drop, the fault must restrengthen during the interseismic period [*Brace and Byerlee*, 1966]. Faults that are stressed continuously by tectonic forces and which exhibit systematic variations in stress drop with recurrence interval may be used to infer the rate of interseismic restrengthening, presuming that the sliding friction during the earthquake is independent of recurrence interval. Based on room temperature friction and static indentation experiments [*Dieterich*, 1972; *Scholz and Engelder*, 1976; *Dieterich and Kilgore*, 1994, 1996; *Goldsby et al.*, 2004], fault strengthening during the interseismic period is thought to result from increases in fault contact area with time due to solid-state deformation (creep) at asperity contacts. However, other laboratory experiments and field observations on exhumed fault zones indicate that solution-transport processes such as pressure solution, crack healing, and asperity contact growth strongly influence fault zone properties and, by inference, the rheology at hypocentral conditions [*Bruhn et al.*, 1994; *Chester et al.*, 1993; *Parry and Bruhn*, 1990]. For many minerals such as quartz, solubility increases with temperature and pressure and at elevated values, if fluid is available, fault zone physical properties can be substantially altered by "solution mass transport." These are processes where minerals sequentially dissolve, are transported, and precipitate because of spatial variations in chemical potential. Differences in chemical potential can arise due to gradients in stress (pressure solution), solid/liquid surface energy (crack healing), or temperature. Significant changes in fault zone permeability and porosity are expected to result from any of these processes. For example, interseismic fault zone fluid pressure could increase with time through the simultaneous operation of crack healing [*Brantley et al.*, 1990] and pressure solution compaction [*Sleep and Blanpied*, 1992], both of which can rapidly reduce permeability. Fault strength may also increase rapidly through increase in load-bearing contact area via contact overgrowths [*Hickman and Evans*, 1992] or pressure solution [*Spiers et al.*, 2004].

Despite these expectations, the rates of these processes in relevant fault zone rocks and minerals are not well constrained. To determine the mechanisms and rates of solution mass transport processes in quartz at the grain scale, we have conducted a series of crack closure, crack healing, and pressure solution experiments using quartz single crystals at temperatures between 350°C and 530°C and at 150 MPa water pressure

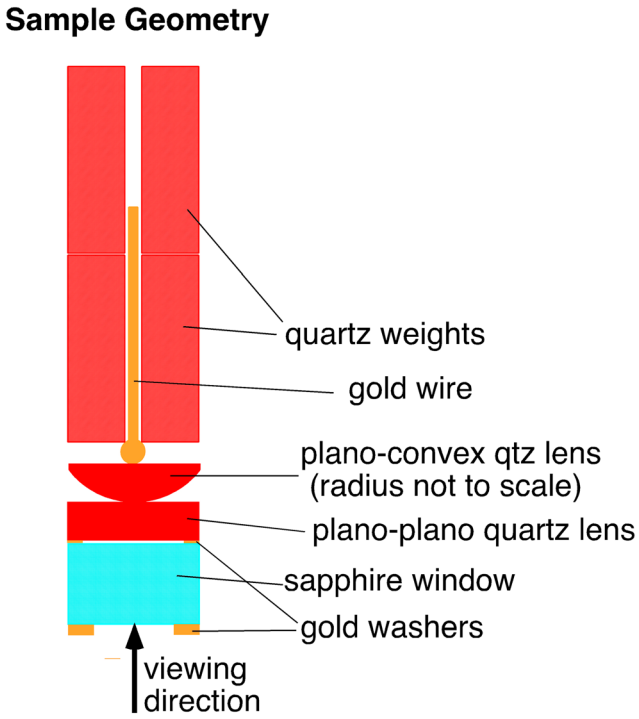

Figure 1. Near-sample configuration consisting of weights, samples, and sapphire window (see also Figure 2), with lenses of synthetic quartz loaded normal to the contact by the quartz weights. The gold wire helps center the load on the contact spot between the two lenses.

[*Beeler and Hickman*, 1996, 2004, 2008; *Hickman and Beeler*, 1999, 1997]. In the present study we quantify the rate of contact overgrowth and compare the results to laboratory data from competing mechanisms of restrengthening. In the absence of fluid flow, overgrowth, called neck growth by *Hickman and Evans* [1992] and in the materials science literature [e.g., *Coblenz et al.*, 1980], occurs in response to strong gradients in surface curvature between the margin of the contact and the open-pore space. Material is dissolved from the high-energy, low curvature wall of an open pore, diffuses through the pore fluid, and precipitates at the low-energy, sharply curved contacts between asperities, cementing them together. In this study we use single contacts with a carefully controlled geometry to provide fundamental constraints on the kinetics of contact growth at the grain scale. The temporal evolution of contact area, adjacent pore volume, and contact convergence were continuously monitored in situ at temperatures between 350°C and 530°C at 150 MPa water pressure in a pressure vessel equipped with an optical observation port. Contact area increases rapidly initially, and the rate decreases monotonically with time. Microstructural observations constrain the rate-limiting process, and a model for growth of asperity contacts [*Hickman and Evans*, 1992] is used to extrapolate the experimental results to predict natural rates of contact growth and fault strengthening at the base of the seismogenic zone.

2. Experimental Technique

The experimental geometry, adapted from *Hickman and Evans* [1992], is designed to access overgrowth while simultaneously preventing the occurrence of pressure solution, crystal plasticity, and strain-induced dissolution effects that can arise in quartz at high temperatures in the presence of water. The asperity is the contact between a convex lens and a flat surface (Figure 1). The stress distribution in the region of contact is known from Hertz's solution [e.g., *Johnson*, 1985] and has the desired property that the normal stress at the contact edge is zero. Loading does not produce high elastic strain energy or plastic yielding at the contact edge that would enhance the solubility there and lead to preferential free-face dissolution, as seen in "indenter" geometries used in some pressure solution experiments [e.g., *Gratier*, 1993]. To avoid pressure solution and crystal plasticity, the loads are low with mean contact normal stresses of less than 2 MPa. Hertzian contact produces a maximum amplification of the mean stress of 1.5 times; therefore, the peak contact stresses are also low.

Experiments were conducted in deionized water, or in one case in air, in a passivated Rene 41 pressure vessel which has a sapphire window in the base (Figure 2). The asperity contacts are constructed by pressing together the two oriented lenses (Figure 1). The lenses were prepared by Boston Piezo-Optics, Bellingham, MA, from quartz crystals synthesized by Sawyer Research Products, Eastlake, OH. In all experiments, the contact lies in the quartz (0001) plane. In one experiment, the flat lens was made of optical grade sapphire rather than quartz.

Inside the pressure vessel, the pair of lenses lies on a thin gold washer above the top face of the sapphire observation window (Figure 1). The gold washer provides a gap that eliminates interference patterns from

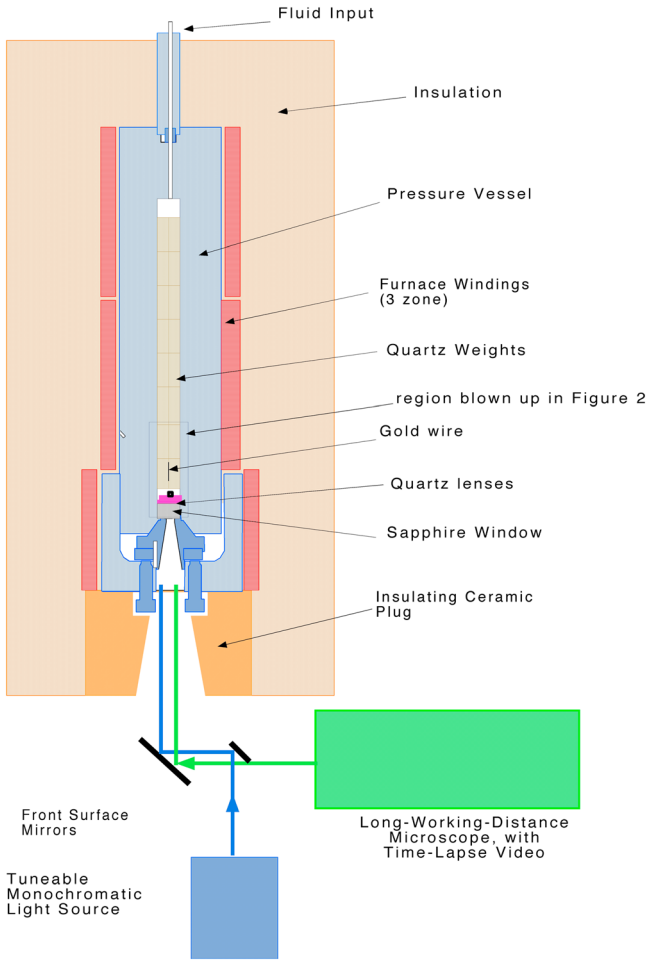

Figure 2. Schematic of experimental apparatus. The pressure vessel has a sapphire observation window directly beneath the samples (see Figure 1), allowing continual monitoring of contact morphology and convergence during the experiments. The long axis of the pressure vessel is vertical. Not to scale.

between the top surface of the window and the bottom surface of the lower lens. The contact is illuminated from below by a tunable monochromatic light source which has a wavelength range of 360 to 600 nm. Both surfaces of the flat lens and the curved surface of the convex lens are ground and polished to an optical finish. The flat side of the convex lens is ground to a frosted finish to reduce back reflections from that interface and other surfaces above it.

Load to the contact was applied by a dead weight consisting of eight cylinders of synthetic quartz. The outer diameter of each weight is a slip fit to the inner diameter of the pressure vessel. Each cylinder was approximately 2.2 cm tall with a mass of approximately 13.5 g. The contact was subjected to a normal load of 0.85 N, resulting in an initial contact radius of approximately 0.4 mm and an average contact normal stress of 1.7 MPa. It is expected that this load is too slight to induce crystal plasticity or appreciable pressure solution. A companion study of curvature-driven crack healing in single crystals of quartz at similar pressure and temperature conditions [*Beeler and Hickman*, 1996] shows crack tip recession rates of 0.006 to 1.0 nm/s for cracks with initial apertures ranging from 3.0 to 20 nm. These rates were used to select a radius of curvature, R_L, for the convex lens (0.7 m) in the present experiments necessary to induce observable healing at the contact assuming neck growth proceeds at rates comparable to crack healing.

The contact was monitored from outside the vessel through the sapphire window using a long-working-distance-microscope equipped with a digital video camera. The camera was recorded with a continuous video recorder, and digital images were periodically captured and used for quantitative determination of contact area and lens convergence using reflected light interferometry (see below). Temperature (±0.2°) within the pressure vessel was measured with a thermocouple inserted through the high-pressure port at the top of the vessel to within an inch of the sample. Fluid pressure (±2 bars) was monitored with an in-line pressure transducer and a pressure gauge. Run conditions are listed in Table 1 and range from 350 to 530°C, all at 150 MPa water pressure, with the exception of a control experiment done dry at atmospheric pressure (0.1 MPa). The samples were raised to these conditions from 22°C and 0.1 MPa over ~2.5 h; temperature was raised from 22 to 100°C, from 100 to 300°C, and from 300°C to the final temperature in three monotonic increments. Fluid pressure increased via thermal expansion over these increments but was manually reduced to keep pressure below a few tens of megapascals over the first two temperature increases and as necessary to keep pressure from exceeding ~100 MPa during the final increment. Pressure was then increased to 150 MPa after the temperature had stabilized. Experiments were quenched from run conditions by reducing the water pressure to atmospheric over a few minutes by venting the fluid and then allowing the open vessel to cool naturally to room temperature. Tables 1 and 2 also show the crystallographic orientation and

Table 1. Asperity Contact Growth Experiments

Experiment	Temperature (°C)	Pressure (MPa)	Duration (h)	Contact Orientation (Quartz)	Grain Boundary Twist Angle (deg)	Initial Load Mass (g)	Recovered Load Mass (g)	Load Change (g)	Initial Sample Mass (g)	Recovered Sample Mass (g)	Sample Change (g)
QNG 3	425	150	413	0001	50	108.344	108.3082	−0.0038	6.8489	6.8498	+0.0009
QNG 4[a]	530	0.1	150	0001	17	108.3149	-	-	6.8612	-	-
QNG 5	530	150	272	0001	17	-	108.271	−0.0044	-	-	-
QNG 6	425 and 530	150	454	0001	47	108.271	108.2389	−0.0321	6.8479	6.8401	−0.0078
QNG 7	350	150	770	0001	18	108.2142	108.1843	−0.0299	6.8507	6.8495	−0.0012
QNG 9[b]	425	150	382	$10\bar{1}0$	-	121.5128	121.488	−0.0248	3.3736	3.3737	−0.0019

[a]In air.
[b]Plano-convex quartz lens on sapphire flat.

relative twist angle of the boundary formed between the two lenses, the latter only for the quartz-on-quartz experiments.

2.1. In Situ Optical Measurements

In the manner of *Hickman and Evans* [1992, 1995], light reflected off the top and bottom surfaces of the lenses interferes, and the interference fringes (Newton's rings) were used to measure the height of the gap between the two lenses, henceforth termed the aperture (Figure 3). Figure 3 is a photomicrograph taken normal to a contact in situ at 430°C and 150 MPa water pressure after 95 h. The contact is the dark circular region that occupies the center of the image. While the contact is circular, in detail, the edge of contact is irregular. The aperture H associated with an interference minimum (a dark fringe resulting from maximum destructive inference) is

$$H = \frac{m\lambda}{2n}, \tag{1}$$

where λ is the wavelength of light, m is the order number, and n is the refractive index of the fluid between the lenses [e.g., *Rossi*, 1965]. A similar equation specifies aperture for interference maxima. Order number was determined by counting outward from the contact and by using the tunable monochromatic light source to position two adjacent fringes (m and $m+1$) acquired at different wavelengths at the same point within the gap between the two lenses and then by simultaneous solution of (1), obtain the expression $m = \lambda_2/(\lambda_1 - \lambda_2)$. The refractive index, required for solution of (1) for H, is

$$n = \sqrt{\frac{2R_m + V_m}{V_m - R_m}}, \tag{2}$$

where V_m and R_m are the molar volume and molar refractivity of water, respectively [*Atkins*, 1982]. The temperature and pressure dependence of (2) is contained in V_m. If R_m and n are frequency independent (no dispersion), $R_m = 3.68\ \mathrm{cm}^3/\mathrm{mol}$ from (2) using n (= 1.333) at room temperature and pressure. Molar volume of water was calculated using the relationship of *Fournier and Potter* [1982] and the tabulated data of *Burnham et al.* [1969]. Using (1) and (2) and the measured temperature, pressure, and interference patterns, H can be determined throughout the experiment.

2.2. Thermal Gradients

To analyze the role of capillarity (surface curvature) in contact growth requires that thermal gradients in the vessel provide negligible driving force for solution transport. The furnace provides relatively uniform heating within the 24.1 cm long vessel bore, with profiling at run temperatures and fluid pressures indicating a maximum temperature variation of 5°C over the entire length and a maximum gradient of 1.2°C/cm. The resulting chemical potential gradient is orders of magnitude smaller than the gradient resulting from surface curvature variations near the contacting asperity; therefore, thermal effects are not expected to influence the reported rates of contact growth.

The lenses and the quartz were weighed before the experiment and again following sample recovery. Changes in mass of the weights are between 0.02 and 0.04% (see Table 1) and reflect dissolution necessary to produce a saturated or near-saturated solution at run conditions. As shown in Table 1, the percentage mass loss for each lens is slightly

Table 2. Symbols and Dimensions

Symbol	Definition	Dimension
H	aperture	m
h	initial aperture	m
λ	wavelength	m
n	refractive index	dimensionless
m	interference fringe order number	dimensionless
R_m	molar refractivity	cm^3/mol
V_m	molar volume	cm^3/mol
A	contact area	m^2
k_-	precipitation rate constant	mol/m^2 s
$\Delta\mu$	chemical potential	J/mol
R	gas constant	J/mol °K
T	temperature (°K)	degrees
Γ_{sl}	solid/liquid surface energy	J/m^2
Γ_{gb}	grain boundary energy	J/m^2
κ	mean surface curvature	1/m
R_L	mean lens radius	m
x	distance from the contact center	m
t	time	s
C_o	concentration in mole fraction	dimensionless
a	contact radius	m
a_0	initial contact radius	m
D	diffusion coefficient	m^2/s
$\nabla\mu$	chemical potential gradient	J/mol m
V	da/dt, growth rate of contact radius	m/s
Q	activation energy	J/mol
ρ	radius of curvature	m
nn	power law exponent	dimensionless
A_T	total contact area	m^2
A_0	initial average contact area	m^2
τ	shear strength	MPa
τ_0	initial shear strength	MPa
b	friction strengthening coefficient	dimensionless
σ_n	normal stress	MPa
μ_0	τ_0/σ_n, initial friction	dimensionless
$\bar{A}$	average contact area	m^2
δ	contact normal rigid displacement	m
u_z	elastic contact normal displacement	m
E	Young's modulus	MPa
ν	Poisson's ratio	dimensionless
p_0	average contact normal stress	MPa
F	empirical constant	m^3/s

higher than for the weights, having a maximum of 0.1%. However, the absolute changes in lens mass are very small, in the range of 1 to 8 mg. While these losses are real, being greater than our measurement precision (±0.0004 g), they are unrelated to contact growth since monitoring of interference fringes during the experiments shows no significant addition or loss of mass from the lens surfaces far from the contact. Furthermore, the losses from the sample do not increase systematically with experiment duration and therefore do not reflect long-term leaching driven by hydrothermal circulation within the vessel.

3. In Situ Observations of Contact Growth and Convergence

Six experiments were conducted, ranging in duration from 150 to 770 h. Two were control experiments, one dry with contact between two quartz lenses at 0.1 MPa air pressure (QNG 4), and another on a wet bimaterial contact (QNG 9, quartz sapphire). All quartz-quartz experiments in water showed contact growth (Figure 4), while the two controls showed no growth (Figure 5). Figure 4 shows successive photomicrographs taken normal to a contact in situ at 430°C and 150 MPa water pressure after 48, 147, and 413 h. The contact is the dark circular region that occupies the center of the images. Qualitatively, the contact can be seen to increase

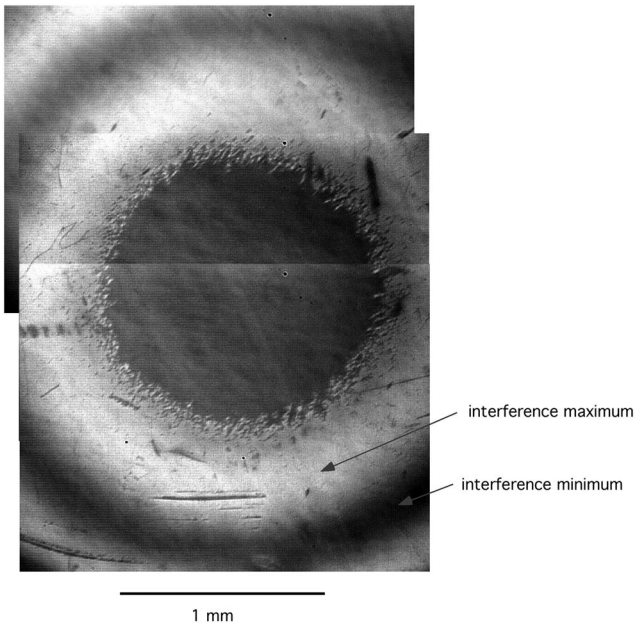

Figure 3. Mosaic of in situ micrographs of the asperity contact from experiment QNG 3 after 95 h at 425°C and 150 MPa water pressure as viewed using reflected monochromatic light (433 nm wavelength). Interference minima and maxima are contours of the thickness of the pore space (aperture) adjacent to the contact between the two quartz lenses, as given in equation (1).

in successive images at longer and longer times. Contact area was digitized from images collected over the entire duration of experiments. Growth of the quartz contacts occurred very rapidly within the first 20 h at run conditions, at rates comparable to those observed in crack-healing experiments in quartz under similar conditions described by *Beeler and Hickman* [1996]. After this, the neck growth rate decreased monotonically with time (Figure 5). The interference patterns were used to monitor convergence. The rate of convergence, here the change in aperture, dH/dt, is related to the outward velocity of the interference maxima and minima dx/dt as dH/dt = dx/dt tan θ, where tanθ is the local slope of the convex lens. To a resolution of 6 nm, no convergence was observed between the lenses in any of the experiments in this study, even when there was significant contact growth (Figure 6). In Figure 6, two mosaics of contact area and the surrounding pore space are superimposed about the contact centerline to simultaneously illustrate contact area change and lack of asperity convergence. Figure 6 (top) shows the contact after 413 h and at (Figure 6, bottom) 123 h. The contact area increased measurably over this time period; however, the interference fringes that directly contour the open-pore space about the contact are stationary. Contact area increase due to deformation at the contact would be recorded by outward migration of the contours by a distance shown by the red arrow. The migration distance was estimated assuming simple removal of material at the contact as would result from pressure solution.

From the lack of convergence or contact area growth in the dry and bimaterial experiments, we conclude that crystal plasticity does not occur at these conditions. From the absence of contact area growth in the dry (quartz-on-quartz) experiment, we conclude that the observed contact area growth in the wet experiments is a fluid-assisted process. From the lack of convergence in the quartz-quartz experiments, we infer that pressure solution did not occur significantly at these low loads and temperatures and more generally that the observed contact growth is not driven by stress. We infer from the control experiment that overgrowths cannot form at the quartz-sapphire contact; perhaps this is because quartz cannot precipitate syntaxially on sapphire and the driving force for capillarity-induced neck growth (i.e., reduction in free surface energy) is absent. Given all of these constraints, in summary, contact growth in the quartz-quartz experiments results from sequential dissolution of quartz from the pore space, transport in solution, and precipitation at the contact margin driven by gradients in the surface curvature, as observed by *Hickman and Evans* [1992] in halite.

4. Models and Interpretation

For a material with isotropic solid-liquid interfacial energy Γ_{sl}, the driving force for transport from surface curvature κ is given by the Gibbs-Thompson relation:

$$\Delta\mu = \kappa\Gamma_{sl}V_m, \tag{3}$$

where $\Delta\mu$ is the chemical potential and V_m is the molar volume. For flat surfaces (κ=0, $\Delta\mu$=0), there is no driving force. In contrast, positive curvature such as the surface of a convex lens has positive energy, while the negative curvature at the margin of the contact (Figure 7) has negative energy relative to a flat surface. To

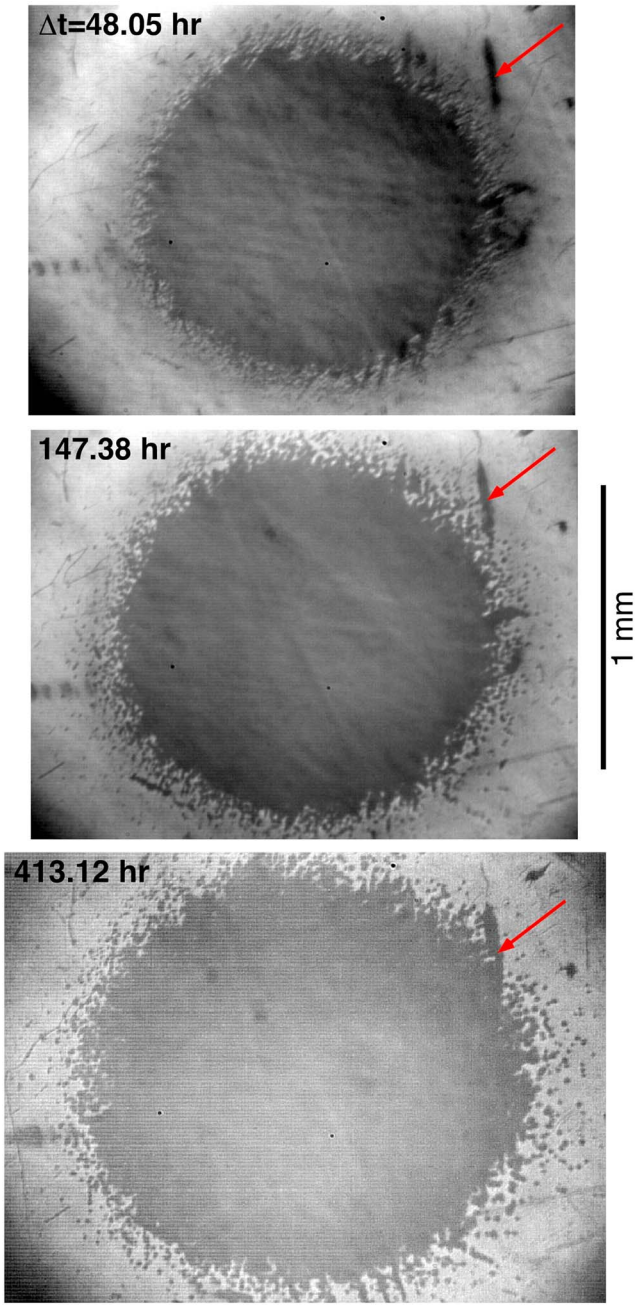

Figure 4. Successive images of contact growth at elapsed times of (top) 48, (middle) 147, and (bottom) 413 h from an experiment (QNG 3) at 425°C and 150 MPa water pressure. Note the roughness of growing contact margin, associated with formation and coalescence of peninsular and isolated contact spots into the growing contact region. Red arrow shows a secondary contact that is gradually incorporated into the principal contact area over time.

minimize energy, the system will tend toward zero curvature by filling in the contact margin using material from the lens surface.

For our asperity contact growth experiments, the driving force is more complicated than equation (3). Quartz has anisotropic solid-liquid interfacial energy due to crystallographic asymmetry. This and the presence of a grain boundary in our experiments require energy terms absent from (3). Nonzero grain boundary energy is expected to decrease the rate of contact growth by increasing the radius of curvature at the contact margin [*Coblenz et al.*, 1980], that is, by analogy to equation (3), to decrease κ. In addition, although the grain boundary plane of each crystal is the same crystallographic plane, there is an in-plane rotational misalignment given by a "twist angle," zero rotation being perfectly aligned. Different experiments have different twist angles (Table 1) that are expected to correspond to different grain boundary energies. We do not have enough data to resolve systematic differences in growth rate with twist angle. Furthermore, there are no data on anisotropy of solid-liquid interface energy for the quartz water system at the conditions of our experiments and no data on grain boundary energy (0001) as a function of twist angle.

The ratio of grain boundary energy to solid-liquid energy may be inferred from the aspect ratio of fluid inclusions trapped on the healed boundary [e.g., *Hickman and Evans*, 1992]. Hickman and Evans were able to quantify these relative energies from grain boundary fluid inclusions in their wet halite-on-halite experiments and found that contact growth rates increased with decreasing grain boundary misorientation, suggesting an influence of grain boundary energy on growth rates. However, they found that if their measured relatively high grain boundary energies were interpreted in the context of *Coblenz et al.*'s [1980] model, then the expected low curvature at the contact margin (i.e., low dihedral angle and high radius of curvature) was not observed. Instead, they saw a high dihedral angle, apparently due to the very high anisotropy in free surface energy exhibited by halite. This suggests that *Coblenz et al.*'s [1980] relation between dihedral angle and near-neck curvature is not applicable to highly anisotropic minerals. Furthermore, dihedral angle is related to the grain boundary energy through a static (equilibrium) or

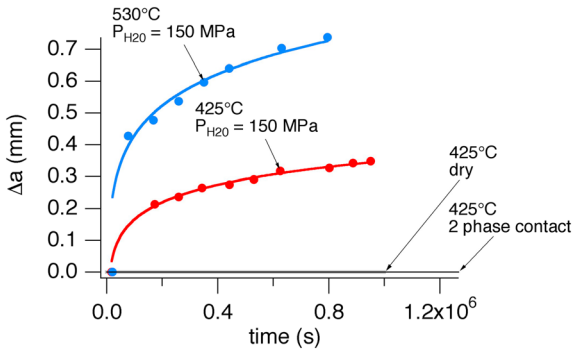

Figure 5. Time-dependent contact growth from four experiments. Contact areas (A) as shown in Figures 3 and 4 were digitized and converted to an equivalent radius $a = \sqrt{A/\pi}$. The change in radius is plotted versus time after subtracting the initial (elastic) contact spot radius. The curves shown are the fits of temporal changes in radius with a general power law. The two control experiments (dry and two-phase contact) show no growth, while the two single-phase wet experiments (red and blue) show rapid temperature-dependent growth.

instantaneous energy balance, whereas near-neck curvature is an evolving, distinctly nonequilibrium microstructure, and the relation between dihedral angle and neck curvature may be more complicated than in *Coblenz et al*. [1980]. Following *Hickman and Evans* [1992], for simplicity, we ignore the effects of the grain boundary and anisotropy and analyze the data using their proposed end-member models of reaction rate and diffusion-limited contact growth.

Hickman and Evans [1992] considered two models where material is sequentially dissolved from the pore space, transported through the pore fluid to the contact margin, and precipitated. Readers interested in the details of these models should consult Appendices A and B of *Hickman and Evans* [1992]. As shown in Figure 7, for one model, the flux of material is limited by the rate of precipitation at the contact, and for the other, the rate is limited by transport through a static pore fluid. For both models, the driving force is the difference in curvature between the relatively flat lens surfaces (solute source) and the contact margin as given by (3). In either model, the overgrowth that occurs at the contact margin is assumed to have a uniform radius of curvature ρ, consisting of a circle tangent to the flat and curved lenses. For precipitation-limited growth (Figure 7a), the rate of precipitation is linearly related to the driving force. Following these assumptions, to first order, the rate of growth of the contact radius is [*Hickman and Evans*, 1992]

$$\frac{da}{dt} \approx \frac{4k_{-}\Gamma_{sl}V_m^2 R_L}{RT(a^2 - a_0^2)}, \tag{4a}$$

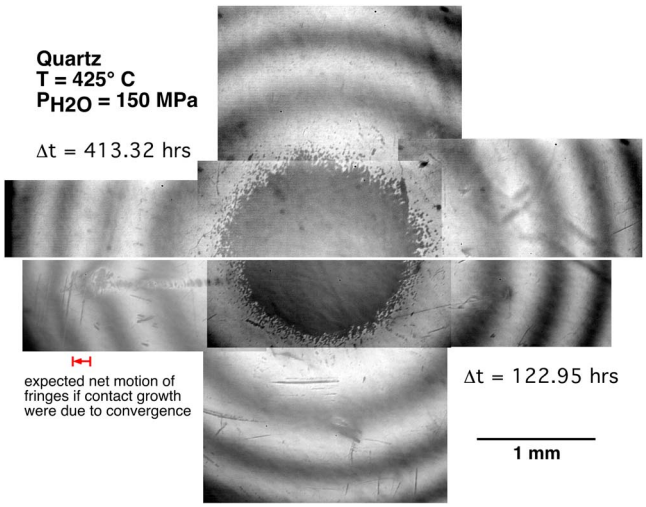

Figure 6. Two mosaics of contact area and surrounding pore space superimposed about the contact centerline in wet quartz-on-quartz experiment QNG 3, illustrating contact area growth over time (neck growth) but without convergence. (top) The mosaic shows the contact after 413 h at 425°C and 150 MPa and (bottom) at 123 h. The contact area (dark region) increased noticeably over this time period; however, the interference fringes surrounding the contact are stationary, indicating no convergence between the two lenses (see text). For comparison, the approximate outward migration of the interference fringes that would result if the observed contract growth were caused by intergranular pressure solution is shown by the red arrow.

where k_{-} is the precipitation rate constant, R_L is the lens radius, R is the gas constant, T is the temperature in °K, a is the contact radius, and a_0 is the initial contact radius. Effectively, the source material for precipitation at the contact margin is assumed to be far from the margin. For a contact radius much less than the lens radius, any value of contact radius can be geometrically related to the initial aperture h at that distance from the center of the contact. See equation (11) and the following text below equation (11) for a discussion of initial aperture from Hertz's solution. For our purposes here, the relation between initial aperture and contact radius is $h = (a^2 - a_0^2)/2R_L$. So the growth rate of the contact (equation (4a)) can be equivalently expressed as

$$\frac{da}{dt} \approx \frac{2k_{-}\Gamma_{sl}V_m^2}{RTh}. \tag{4b}$$

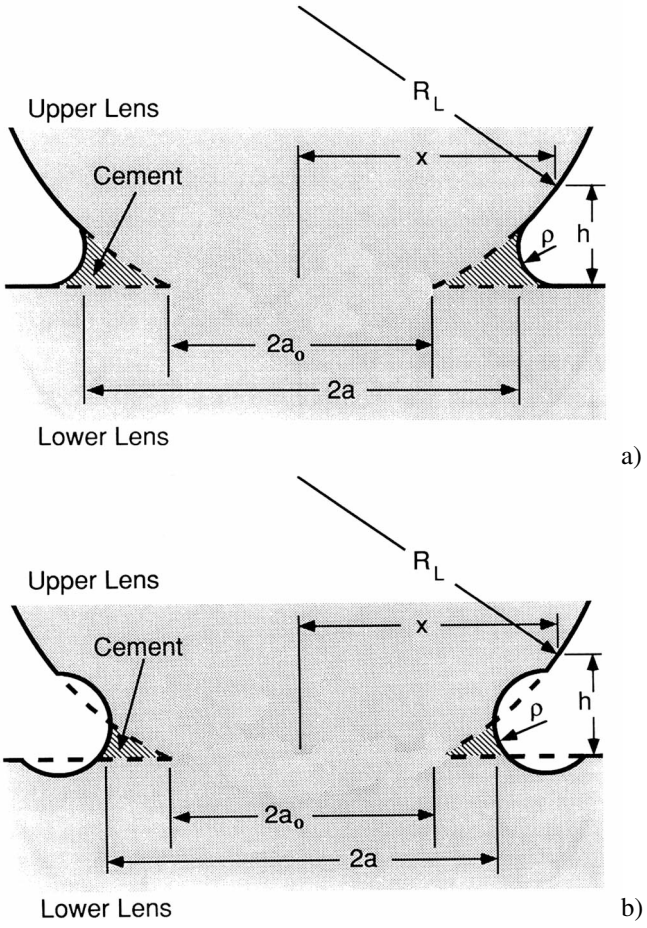

Figure 7. Schematic representations of end-member models of asperity contact growth, modified from *Hickman and Evans* [1992]. R_L is the lens radius, ρ is the radius of curvature at the neck, a is the contact radius, a_0 is the initial contact radius, x is the distance from the contact center, and h is the initial aperture. (a) Precipitation-rate-limited growth, characterized by an inverse dependence of growth rate on h. (b) Diffusion rate-limited growth, which is characterized by local dissolution pitting and growth rate depending on $1/h^2$.

For the diffusion-limited model, the driving chemical potential gradient is defined as the difference between the source and sink potential given by (3) divided by the transport distance. The source is further assumed to be local and approximated by an annular region of uniform circular cross section (Figure 7b). To the first order, these assumptions result in a contact radius growth rate of [*Hickman and Evans*, 1992]

$$\frac{da}{dt} \approx \frac{\pi D C_0 \Gamma_{sl} V_m a}{RTR_L h^2}, \tag{5}$$

where D is the diffusion coefficient of the solute in the fluid and C_0 is the concentration of solution in equilibrium with a planar interface.

To distinguish between these end-member models, the time histories of contact radius were fit using a general power law (example fits are shown in Figure 5). The contact radius was determined by digitizing the contact area A from the captured images, and the area was used to calculate an equivalent radius using $a = \sqrt{A/\pi}$. Initial contact area (and, hence, a_0) is estimated using Hertz's solution (see equation (11) below) [*Johnson*, 1985]. We first verify the consistency of the interference pattern with Hertz's prediction using the static load from the quartz weights and top lens, corrected for buoyancy at the appropriate temperature and water pressure. The derivative of the fit is the growth rate. This neglects small-scale heterogeneities in growth rate (e.g., as seen in Figures 3, 4, and 6) and yields, in effect, an average radial growth velocity for each experiment. Then we fit these contact growth rates to a power law function of initial aperture, h, $da/dt \propto h^n$, as in (4a), (4b), and (5) (Figure 8). Fits to the velocity versus aperture data (Figure 8) produce exponents in the proportionality between da/dt and h^n of $n = -2.1$ to -2.3, which are close to the ideal $n = -2$ expected for diffusion control (equation (5)).

While this comparison of diffusion and reaction rate models favors diffusion, the diffusion model used relies on the assumption that the radius of curvature at the contact edge is half the maximum diffusion distance. A concern is that rather than agreement with a solution to the diffusion equation, we have agreement with a model that contains an imposed geometric constraint on diffusion. Thus, conclusions drawn from this model are not a definitive indicator of the role of diffusion in these particular experiments.

4.1. Temperature Sensitivity

These experiments were specifically conducted to characterize the temperature dependence (Table 1), and the combined data set shows a strong temperature effect (Figure 8). The first experiments were run at 425 and 530°C (QNG 3 and QNG 5), followed by a temperature stepping experiment (QNG 6) over the same range. These three tests provide our best constraint on the temperature sensitivity of contact area growth. To empirically quantify the effect, we follow a convention in rock mechanics [e.g., *Chester*, 1995; *Nakatani*, 2001]

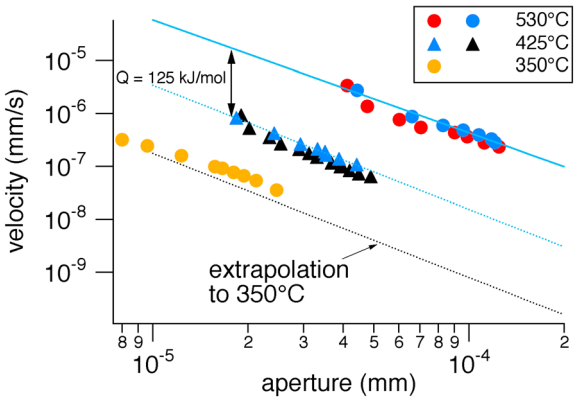

Figure 8. Velocity of contact growth in wet quartz/quartz experiments (d*a*/d*t*) plotted against local aperture. Velocity is the slope of contact radius versus time from fits, such as shown in Figure 5 for each experiment. The initial aperture is that at the edge of the contact. The velocity decreases with initial aperture for all experiments. Experiments QNG 5, 3, and 7 were conducted at constant temperatures of 530, 425, and 350°C, respectively, and QNG 6 contained a temperature step from 425 to 530°C. Fits to the data (blue lines) at 425 and 530°C using a general power law relation between growth velocity and initial aperture (see text) yield an aperture exponent $n = -2.1$ to -2.3. The implied apparent activation energy from experiments at 530 and 425°C is ~125 kJ/mol, which upon extrapolation using an Arrhenius temperature dependence (black dotted line) predicts the observations at 350°C reasonably well.

and estimate the apparent activation energy Q assuming an Arrhenius relation $V = da/dt \propto \exp(-Q/RT)$. The activation energy inferred from experiments at two different temperatures T_1 and T_2 is

$$Q = R\left[\frac{T_1 T_2}{T_1 - T_2}\right]\log\frac{V_1}{V_2}. \quad (6)$$

Q so-determined is approximately 125 kJ/mol. The observed rate of contact growth in a later experiment conducted at 350°C is reasonably well predicted by extrapolation based on this activation energy (Figure 8), although it slightly underpredicts the rate.

This apparent activation energy is not consistent with the analysis of the *Hickman and Evans*'s [1992] models in the previous section that suggests that contact growth is diffusion rate limited. One hundred twenty five kilojoules per mole is much higher than expected if the rate of contact growth was determined solely by diffusion through a bulk fluid. For example, an activation energy of 19 kJ/mol was determined by *Ildefonse and Gabis* [1976] for diffusion of silica in bulk water at 100 MPa pressure and 550°C. The apparent activation energy is also nearly twice that expected if the rate of contact growth was determined by precipitation kinetics alone. *Rimstidt and Barnes* [1980] find that the rate constant for dissolution of quartz has an activation energy of 67 to 75 kJ/mol at temperatures between 25 and 300°C.

It is possible that the measured apparent activation energy reflects complications associated with diffusion within the narrow near-contact aperture in these experiments. Thin water films may be more structured, requiring a higher activation energy [*Farver and Yund*, 1999]. Unfortunately, the energy difference required to explain the apparent activation energy is much larger than would be expected based on the available previously published experimental diffusion data. For example, *Farver and Yund* [1999] found an activation energy of 30 kJ/mol for isotopic exchange along interphase boundaries between wet quartz and mica at comparable temperatures, which they attributed to oxygen diffusion through a structured water film. Although this is a modest increase over diffusion in bulk water, our apparent activation energy is more than 6 times larger than in bulk water and is closer to that expected for solid-state grain boundary diffusion in quartz [e.g., *Farver and Yund*, 1991]. An additional problem with invoking a structured fluid film to explain the activation energy is that the film thickness estimated by *Farver and Yund* [1999] was much smaller, at 2 nm, than the near-contact aperture in our experiments, which we estimate to be in the range of 8 to 100 nm. Therefore, it is likely that the intergranular fluid film in this study would have been much less structured than expected for the much thinner films inferred by Farver and Yund [c.f., *Rutter*, 1976]. While the comparison is further complicated by differences in the diffusing species, oxygen compared to silica, at present, we have no reason to believe that our results reflect the influence of a structured water film.

Given that the inferred activation energy will depend on the particular model equation used, it is probably unwise to attach physical significance to the apparent activation energies derived from (6). At present, the reason for the high activation energy is not known, although the value is well determined and should be adequate for extrapolation of the data from these experiments beyond their temperature range. The physical basis for the particular temperature dependence remains a topic for future investigation with a more extensive data set.

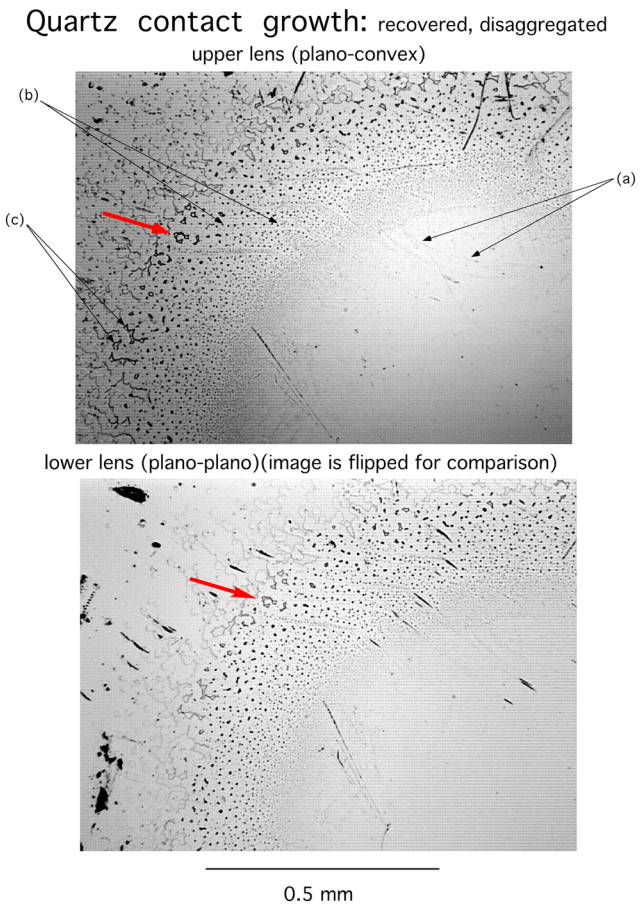

Figure 9. Reflected light photomicrographs of recovered contact from wet quartz-on-quartz experiment QNG 3 that has been broken along the midplane of the contact, showing contact margin surrounding healed grain boundary microstructure. The center of the contact is located approximately in the lower right corner of each image. The grain boundary contains matching fluid inclusions evident on each side of the recovered lens pair. (top) The plano-convex lens and (bottom) the plano-plano lens flipped horizontally for comparison. For reference the red arrows point to the same feature on the top and bottom lenses. The features labeled with a, b, and c are discussed in the text.

5. Microstructures From Recovered Samples

The dominant microstructural feature resulting from contact area growth is the formation of fluid inclusions in the contact grain boundary. Only the largest inclusions are visible in situ at relatively low magnification (Figure 4). Fortunately, the cemented contact spots in the wet quartz-on-quartz experiments have enough cohesive strength to remain welded together after the experiment is over and the samples are recovered intact from the vessel. This allows us to make additional observations of inclusion geometry and distribution using standard optical and scanning electron microscope (SEM) techniques. Figure 9 shows reflected light images of a recovered quartz-on-quartz contact in the vicinity of the contact margin. The lenses have been separated through the midplane of the contact. Figure 9 (top) is the convex lens, and Figure 9 (bottom) is the flat lens flipped horizontally for comparison. Inclusion size increases with distance from the center of the contact. Toward the contact center are aligned trains of inclusions, such as that between the ends of the arrows labeled (a) on Figure 9 (top); these probably define the location of the deepest polishing scratches on the lenses prior to healing (also see Figure 10d). There are trains of larger inclusions, like those between the arrow heads labeled (b) farther out toward the contact margin. These coincide with linear features that developed during the early stages of healing. These are also visible in the contact margin in Figure 4 (top, at 48 h). These inclusions in the recovered sample have annealed to an equilibrium shape. However, the very large inclusions toward the outer perimeter of the contact, such as those at the ends of the arrows labeled (c) in Figure 9, have extremely irregular shapes. Similarly, the red arrows in Figure 9 point to the same irregular inclusion mirrored on each lens. The contact margin is very irregular, and there are small regions of contact well outside of the large contiguous contact, as shown in the in situ images in Figure 4. As the irregular contact margin grows and the regions of discontinuous contact also expand, they intersect isolating inclusions of very irregular shape. If given enough time at the experimental conditions, the inclusions with initially irregular geometry would presumably evolve to a regular shape that minimizes surface energy.

Although not apparent at petrographic magnification (Figure 9), the process of inclusion formation extends over the entire healed grain boundary. Figure 10 shows a series of five high-magnification SEM images from a transect across the same recovered contact as shown in Figure 9. The density of inclusions decreases, and their size increases with distance from the contact center, and even the center of the contact is covered with inclusions (Figure 10e). From these images, the largest equilibrium-shaped inclusions appear to be faceted in a trigonal pyramid (Figure 10b) as expected from the crystallography of quartz and the orientation of the

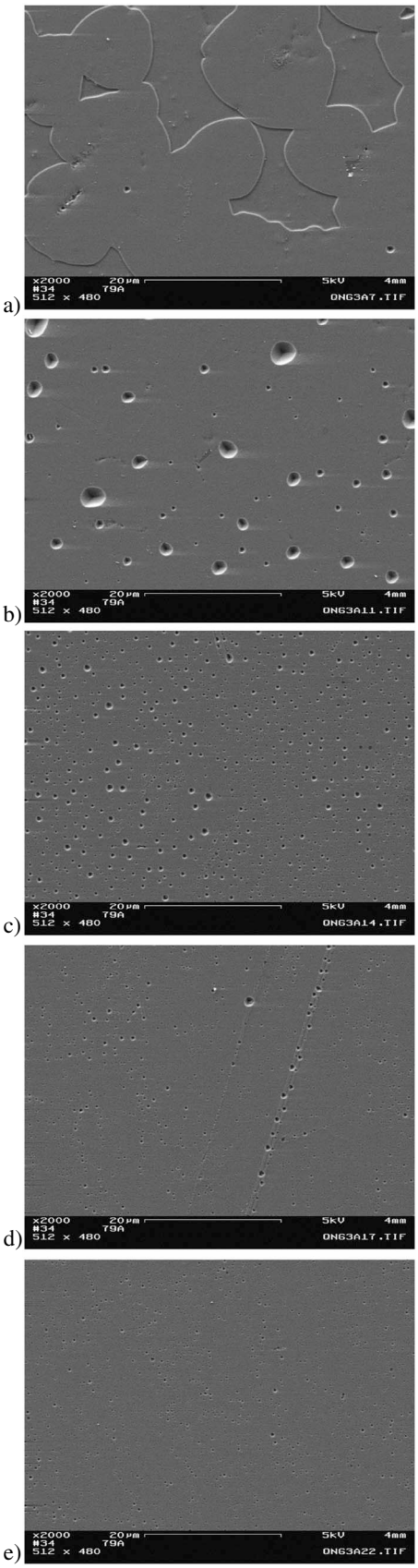

grain boundary (0001), being normal to the *c* axis. The pyramid facets in the inclusions would then logically be (1011), although we have not confirmed this orientation in our experiments. The existence of inclusions over the entire grain boundary suggests that at these experimental conditions, the contact is not uniformly wetted by fluid. In particular, by considering the balance of Γ_{sl} and grain-boundary energy (Γ_{gb}) under equilibrium conditions, the necessary condition for the existence of isolated fluid inclusions along an otherwise dry grain boundary is $\Gamma_{gb}/\Gamma_{sl} < 2$ [*Hickman and Evans*, 1992]. Reasonably, the dry grain boundary energy is less than twice the solid-liquid interfacial energy in these experiments.

The structure of the pore space directly adjacent to the contact is consistent with a model of diffusion-limited growth rather than a model limited by the dissolution/precipitation reaction. Images of the margin of a recovered contact illuminated in reflected white light on a petrographic microscope (Figure 11) show the unique shape of the near-contact aperture. In white light the interference pattern consists of ordered colors. For increasing aperture, such as generally shown in Figure 11, the colors increase from dark at zero aperture to white near the contact edge to red-blue-green-yellow in sequence as aperture widens to the left in this figure. Then the sequence of red-blue-green-yellow repeats twice more. Each repeat is a change in order as the aperture continues to increase. These can be used quantitatively to determine aperture. In contrast to this general trend of widening of aperture with distance from the contact, close examination of the aperture immediately adjacent to regions of contact in the right third of this image shows highly localized enlargements in aperture, indicated by increases in color order. The two arrows are included to direct attention to these features. First, consider the region directly adjacent to the irregular contact indicated by the lower right arrow. For a smooth lens, corresponding to the starting condition in these experiments, the aperture should monotonically increase with distance from the contact, starting with very small

Figure 10. Five SEM images from a transect across the surface of one half of an asperity contact pair from experiment QNG 3 progressing from the contact edge to the contact center. Note that the scale bar for each image is 20 μm. (a) Contact edge with irregular pores. (b) Large equilibrium-shaped pores from inside the contact. (c) Smaller pores, some in aligned trains. (d) Near the contact center. Note the clear train of larger pores; these are interpreted as resulting from healing of a large scratch on the initial lens surface. (e) Contact center showing very small isolated pores. The entire contact region is marked by isolated pores that increase in size outward from the contact center. The presence of pores within the contact or grain boundary suggests that at run conditions, healing of the initial grain boundary and subsequent contact growth produced a solid-state (dry) grain boundary containing isolated fluid inclusions.

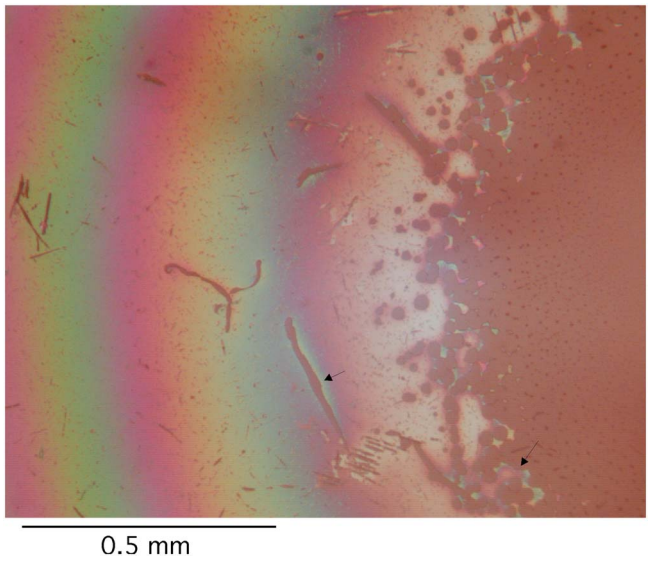

Figure 11. Reflected white light image of an intact contact recovered from experiment QNG 6 taken in air. Since the two quartz lenses used in this experiment are still welded together, the white light interference pattern shown here can be used to determine localized changes in aperture between the two lenses near the perimeter of the intergranular contact (dark region along the right third of image). This white light interference pattern consists of ordered colors, proceeding outward from the first-order white near the contact region to the high-order distinct colors as the aperture widens to the left. As shown by the two arrows, local enlargements of aperture ("moat" formation) immediately adjacent to the contact result from free-face dissolution and provide microstructural evidence for diffusion-limited solution mass transport (see text).

apertures indicated by first-order interference colors at the contact edge. Instead, the contact margin is associated with a higher-order color, indicating that the aperture is anomalously wide directly adjacent to the contact. Similarly, the left arrow in Figure 11 shows a region immediately adjacent to a secondary contact, which is separated from the main contact and was likely nucleated at a surface flaw in one of the lenses. The similarity of interference colors adjacent to this secondary contact and those farther to the left (where the aperture is larger) indicates that the aperture adjacent to this contact has been locally enlarged. These features reflect local free-face dissolution at contact margins and are ubiquitous in the recovered samples. By analogy to the *Hickman and Evans*' [1992] diffusion rate-limited model (Figure 7a), the widening of aperture near the contact reflects locally dissolved quartz as the source material for the asperity contact overgrowth. This microstructure is a definitive indication of diffusion-limited growth.

6. Extrapolation of Contact Growth Rates to Faults

To determine the potential role of asperity contact growth on rough fault surfaces at hypocentral conditions, we extrapolate our hydrothermal laboratory measurements of contact growth to the much smaller asperity contact sizes appropriate for laboratory-scale fault surfaces. That is, we make a comparison between our experiments that measure the rate of contact overgrowth of truly static contacts where there are no changes in shear nor normal components of strain, and friction experiments where strength recovery results from increasing contact area due to normal and perhaps shear yielding of highly stressed asperity contacts. The purpose of the comparison is not to argue that contact overgrowth is more important than yielding or pressure solution in nature but simply to compare the relative rates using the same contact dimension. We then extrapolate our data to natural faults through comparison with seismological observations of small earthquakes made in deep boreholes and mines.

6.1. Friction Data

The tendency for a frictional fault surface to restrengthen with time is conventionally measured indirectly in a slide-hold-slide test [*Dieterich*, 1972]. In the test the sample is slid initially at a steady state velocity, then the loading velocity is set to zero. The measured strength then relaxes as in a conventional stress relaxation test. Although the loading velocity is zero, the sliding velocity of the fault is not zero because the shear stress remains high, and ongoing fault slip relaxes the elastic distortion of the testing machine. After some length of time, the sample is reloaded by resetting the load point velocity to the original rate, the fault strength increases, reaches a peak, and subsequently returns to its previous steady state value. The amount of strengthening that has occurred during the relaxation as measured by the peak is linear with log of hold time and is presumed to be controlled by an underlying time-dependent process [*Dieterich*, 1972]. In physically motivated rate and state friction formulations, the apparent rate of log time-dependent strengthening is characterized by a coefficient *b*.

This is the log rate of contact area increase associated with normal yielding of the contact asperities under conditions of nonzero shear slip rate in the plane of asperity contact [*Dieterich*, 1978, 1979].

To compare our direct measurements of true static asperity contact growth to those implied by laboratory friction data [*Dieterich*, 1972, 1978], we express the friction data in terms of contact area change using friction theory following *Tullis and Weeks* [1987]. Consider the total real area of contact on a fault surface A_T as being a function of time of contact $f(t)$ via some unknown process, be it growth driven by surface curvature or a solid-state process such as indentation creep:

$$A_T = N(A_0 + f(t)), \tag{7}$$

where A_0 is the average initial ($t = 0$) contact area and N is the number of contacts. Since we wish to compare rates of increase in contact area from our hydrothermal experiments with those predicted by time-dependent "frictional strengthening" [e.g., *Dieterich*, 1972], assume that the real area of contact is to first-order fixed by ductile yield strength of the contact population. In this case, for a given A_T, the product NA_0 is a constant. Comparing the general expression for how area of contact changes with time (equation (7)) to low-temperature slide-hold-slide tests, where the fault strength increases during "static" contact, fault shear strength is given by [*Dieterich*, 1972, 1978]

$$\tau = \tau_0 + b\sigma_n \ln(t + 1), \tag{8}$$

where τ_o is the initial shear strength, σ_n is the normal stress, and b is an empirical constant. Assuming that shear strength is proportional to the total area of contact, $\tau = CA_T$ with a constant of proportionality C, and equating (7) and (8) at $t = 0$ yields $C = \tau_0/NA_0$. Substituting back into (8) results in

$$A_T = NA_o\left[1 + \frac{b}{\mu_0}\ln(t + 1)\right], \tag{9}$$

where $\mu_0 = \tau_0/\sigma_n$. Defining the average single contact area as $\bar{A} = A_T/N$, average contact area evolves with time relative to the initial contact area in friction hold tests as

$$\frac{\bar{A}}{A_0} = 1 + \frac{b}{\mu_0}\ln(t + 1). \tag{10}$$

This is the normalization of friction data proposed by *Tullis and Weeks* [1987] and essentially identical to that used by *Goldsby et al.* [2004], *Beeler* [2007], *Boettcher et al.* [2007], and *Beeler et al.* [2007] to compare friction data with other independent laboratory measurements of contact area and contact-scale rheology.

6.2. Hydrothermal Data

Measuring contact area increase on laboratory time scales in hydrothermal experiments required a relatively large starting contact and narrow adjacent aperture. The radius of curvature necessary to produce an initial contact diameter of 0.8 mm is 4.72 m, and the initial contact normal stress was 1.7 MPa. These contact-scale conditions are very different from those at contacts on a bare rock frictional surface, where the contact radius (~d_c in rate-and-state friction) is a few microns and the contact normal stress is the material yield strength [*Dieterich and Kilgore*, 1994, 1996]. To extrapolate to conditions appropriate to rock friction, we use a Hertz's contact model [*Johnson*, 1985]. While the Hertz's solution is only strictly applicable to elastic displacements, it provides a simple analytical model with which to calculate the near-contact aperture necessary for estimating the rate of asperity contact overgrowth. At zero applied load, aperture at distance x from the contact center in the ball-on-plate geometry (Figure 2) is $h_{\text{noload}} = R_L - \sqrt{R_L{}^2 - x^2}$. Upon application of load, Hertz's model predicts relative displacement between the two lenses in the z direction normal to the contact to be $\delta = a_0{}^2/R_L$, with a near-contact normal deflection $2u_z$. The aperture prior to the onset of asperity contact growth is [*Johnson*, 1985]

$$h = h_{\text{noload}} - \delta + 2u_z \tag{11}$$

with

$$u_z = \frac{(1 - \nu^2)p_0}{2Ea_0}\left\{(2a_0{}^2 - x^2)\sin^{-1}\left(\frac{a_0}{x}\right) + x^2\left(\frac{a_0}{x}\right)\sqrt{\left(1 - \left(\frac{a_0}{x}\right)^2\right)}\right\} \quad x > a_0\,,$$

where ν is the Poisson's ratio, E is the Young's modulus, and p_0 is the average contact normal stress. To extrapolate to arbitrary contact stress and asperity contact size, p_0 and R_L are selected to produce an initial

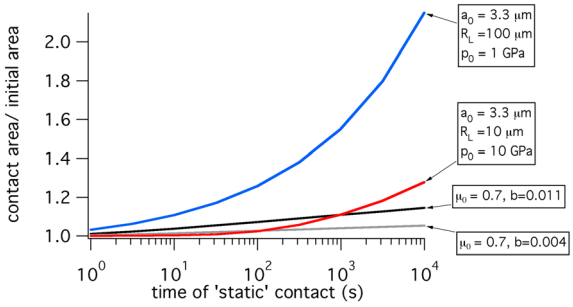

Figure 12. Comparison between extrapolated rates of contact asperity growth indicated by our experiments and fault strengthening rates derived from laboratory friction and healing experiments conducted by other investigators. The red and blue lines are the data from this study extrapolated to a typical laboratory asperity contact size (3.3 μm) using simple Hertzian contact theory, for the contact curvatures and effective normal stresses shown (see text, after *Johnson* [1985]). The gray and black lines, respectively, are the contact growth rates derived from friction experiments conducted at room temperature on bare surfaces of quartzite [*Dieterich and Conrad*, 1984] and at hydrothermal conditions on quartz powders [*Chester*, 1995; after *Chester and Higgs*, 1992].

contact radius $a_0 = p_0 \pi R_L (1 - \upsilon^2)/E$ [*Johnson*, 1985], determining the initial aperture calculated from (11). The change of aperture with time is $da/dt = F/h^2$, where F is an empirical constant determined from the experiments (Figure 8).

6.3. Discussion of Contact Growth Extrapolation

The friction simulations with (10) use two sets of parameters. The first are from room temperature experiments on quartzite at 1.7 MPa normal stress ($b = 0.004$ [*Dieterich and Conrad*, 1984]); the second from hydrothermal experiments on quartz gouge at temperatures between 57 and 450°C and 20 to 150 MPa effective normal stress ($b = 0.011$ [*Chester*, 1995]). These values along with a nominal friction, $\mu_0 = 0.7$, are used to estimate area change (Figure 12). We conducted numerical simulation of contact area growth from our wet quartz-on-quartz contact growth experiments with $p_0 = 1$ and 10 GPa and R_L set to 100 and 10 μm, respectively. This choice of parameters produces $a_0 = 3.3$ μm in both cases, as appropriate for d_c in bare rock friction on smooth surfaces [see *Paterson and Wong*, 2005]. The 425°C data are consistent with $F = 9.954 \times 10^{-8}$ μm^3/s. Using this value at the contact stress of 1 GPa, predicted contact area and rate of area increase greatly exceed those of both the room temperature and hydrothermal friction data (Figure 12), and at the longest times, the rate of increase is orders of magnitude higher. Using the higher contact stress of 10 GPa, a value equal to quartz yield strength produces lower rates of growth because the aperture is initially wider at the contact margin. Nonetheless, after 1000 s, the growth and growth rate exceed the rate of frictional strengthening inferred from room temperature and hydrothermal friction data.

Extrapolating strengthening rates (blue and red curves in Figure 12) to time periods appropriate to earthquake recurrence indicates that growth rates for fluid-assisted contact growth exceed those from solid-state creep by orders of magnitude, at least for natural faults with asperities of similar size to those treated in our extrapolation. Seismological observations in deep mines such as the Natural Earthquake Laboratory in South African Mines project [*Boettcher et al.*, 2009] and in the San Andreas Fault Observatory at Depth borehole [*Ellsworth and Imanishi*, 2008] infer that $M -2$ and smaller earthquakes have asperity contact dimensions on the order of 10 μm; thus, the importance of solution-transfer healing suggested that the overgrowth experiments could well apply to these very small earthquakes. It may also be true that the onset of earthquake slip on much larger-magnitude earthquakes is controlled by regions of the fault with asperity contact dimensions of this size, as seems to be the case for the 2004 Parkfield earthquake [*Johnston et al.*, 2006]. Based on this simple extrapolation, fault strength recovery at and near the base of the seismogenic zone, even for much larger earthquakes, may be dominated by hydrothermal over "frictional" processes.

In a previous study of strength recovery at more modest temperatures, *Nakatani and Scholz* [2004, 2006] suggested that hydrothermal effects dominate strength recovery at temperatures as low as 200°C in quartz at 100 MPa effective normal stress and pore pressure of 10 MPa. Our results at significantly higher temperatures and fluid pressures are consistent with this interpretation. Keeping in mind that our experiments are diffusion rate limited, along any fault in the Earth where there is significant fluid flow leading to the influx of supersaturated solutions, fault healing rates due to hydrothermal contact growth will be even faster than our extrapolation. Nevertheless, there are limitations to our comparison between overgrowth and frictional strength recovery, and significant differences in conditions are different between the two types of experiments, notably the stress state. Friction hold tests are conducted at high shear resistance, meaning that the contact shear stresses are at their shear and normal yield strengths [e.g., *Dieterich and Kilgore*, 1994,

1996; *Nakatani*, 2001], whereas our experiments are conducted at low normal stress and no shear stress. Given these differences and the unknown source conditions of natural seismic faults, it is not possible to argue whether contact overgrowth or crystal plasticity are more important for natural faults solely on the basis of the comparison.

7. Implications for the Recovery of Coseismic "Damage"

In terms of the driving force, contact overgrowths are little different from crack healing [*Hickman and Evans*, 1987; *Brantley et al*., 1990], the tendency for dilatant fractures to fill over time due to curvature-driven flux. Likely to the first order, the rate of crack healing for quartz can be estimated from our asperity growth data. One important application is to the recovery of the so-called damage zones of moderate and large earthquakes. Active seismic source studies show increases in wave speed following large earthquakes that continue for many years postseismically [e.g., *Li et al*., 1998; *Li and Vidale*, 2001]. The increases that apparently occur within a broad, hundreds of meter wide zone are evident as fault zone trapped waves and decreases in trapped *P* and *S* wave arrival times. Increases in wave speed over the decade following the 1992 Landers and 2004 Parkfield earthquakes are around 0.5 to 1%/yr with the rate decreasing with time [*Li et al*., 1998, 2006; *Li and Vidale*, 2001]. The wave speed changes are attributed to a mechanism of "strengthening" or "healing" of the fault zone following the earthquake via the progressive closure of coseismically generated cracks presumed to be created as the earthquake rupture front propagates by, as in dynamic rupture simulations [*Andrews*, 2005]; hence, they are attributed to damage. There is some evidence that the so-imaged damage extends to near the base of the seismogenic zone [*Li and Malin*, 2008; *Wu et al*., 2010] and persists even for events with recurrence times of thousands of years [*Cochran et al*., 2009]. Nonetheless, and despite the association of these zones with coseismically generated dilatant cracks in conceptual models and as represented in numerical simulations as inelastic deformation, more exactly, these are elastic contrasts with unknown physical origin. For example, is the time-dependent change observed in a "damage zone" closure of coseismic-generated dilatancy or is it changes in elastic properties due to postseismic time-dependent fluid flow? Similarly, if elastic contrasts defining the deeper extent of the fault zone are due to coseismic dilatancy, then why do they also appear in the creeping section of the San Andreas [*Wu et al*., 2010; *Ellsworth and Malin*, 2011]? Might instead the damage be a zone of alteration associated with the fault?

Because the experiments in the present study define the rates of curvature-driven cementation of porous materials, and the temperature dependence of the process, they can be used to place bounds on the rate of "strength" recovery due to crack healing. An implication of the data is that healing of dilatant porosity is significantly more rapid at depth than near the surface, meaning a strong depth dependence to the fate of any coseismically generated porosity, permeability, and the associated elastic contrast. Although specific calculations are beyond the scope of our experimental study, since the creation of dilatancy is suppressed at elevated confining pressure in the first place, because crack healing is strongly aperture dependent, and its rate increases by approximately 1 order of magnitude per 100°C (Figure 8), it seems unlikely that significant coseismically generated dilatancy is maintained over the earthquake cycle near the base of the seismogenic zone.

8. Conclusions

Experiments conducted using polished bicrystals of quartz in an optical hydrothermal reaction vessel indicate that asperity contact growth due to capillarity-driven mass transfer occurs rapidly in quartz at temperatures between 350 and 530°C and 150 MPa water pressure. No intergranular convergence was observed in these experiments in which the effective contact normal stress was low (1.7 MPa). This observation plus the lack of convergence in a dry control experiment indicate that neither crystal plasticity nor intergranular pressure solution contributed to the observed contact growth. The grain boundary structure formed during these experiments is solid-state, containing isolated fluid inclusions. Microstructural observations indicate that contact growth is diffusion rate limited, with free-face dissolution in proximity to the growing contact as the source of the overgrowth. Contact growth is thermally activated with an apparent activation energy of ~125 kJ/mol, much higher than that for diffusion in fluid and higher than the activation energy for quartz precipitation/dissolution. The reason for this high activation energy is unknown.

We expect that fault strengthening in nature involves contributions to asperity contact area growth from crystal plasticity, pressure solution, and contact overgrowth. Our study is the first to quantify the rate of restrengthening due to contact overgrowth for quartz, albeit in idealized single-contact experiments, and to put the measured rate in context of laboratory data from competing mechanisms. When extrapolated to the higher contact normal stresses and smaller contact sizes of laboratory rock friction tests, our measured rates of contact area growth imply fault strengthening through capillarity-driven diffusive mass transfer at rates orders of magnitude higher than measured in room temperature and hydrothermal friction experiments. The comparison allows the possibility that contact overgrowth is an important fault restrengthening mechanism at the deepest extent of natural seismic faults.

Acknowledgments

All of the data generated in the experiments in this study, such as those displayed in Figures 5 and 8, are available from the corresponding author (N.M.B.). This study would not have been completed without the assistance, advice, and borrowed equipment of Brian Kilgore and John Pinkston. The manuscript was greatly improved in response to comments by Diane Moore, Yousif Kharaka, Wendy McCausland, and Evelyn Roeloffs. We are indebted to Sue Brantley and Kevin Shelton for sharing unpublished interpretations and observations from their previous studies of crack healing and fluid inclusion formation in quartz. Many thanks to Norm Beniot Sr. of Boston Piezo-Optics for manufacturing the lenses, technical assistance, and providing background on synthetic quartz. The SEM images were obtained with guidance from Robert Oscarson. Thanks to Terry Tullis and Brown University for the use of their computing facilities.

References

Andrews, D. J. (2005), Rupture dynamics with energy loss outside the slip zone, *J. Geophys. Res.*, *110*, B01307, doi:10.1029/2004JB003191.

Atkins, P. W. (1982), *Physical Chemistry*, 1095 pp., W. H. Freeman, San Francisco, Calif.

Beeler, N. M. (2007), Laboratory-observed faulting in intrinsically and apparently weak materials: Strength, seismic coupling, dilatancy, and pore fluid pressure, in *The Seismogenic Zone of Subduction Thrust Faults*, edited by T. Dixon and C. Moore, pp. 370–449, Columbia Univ. Press, New York.

Beeler, N. M., and S. H. Hickman (1996), Crack healing in quartz: Experiments and theoretical considerations, *Eos Trans. AGU*, *78*, F696.

Beeler, N. M., and S. Hickman (2004), Stress-induced, time-dependent fracture closure at hydrothermal conditions, *J. Geophys. Res.*, *109*, B02211, doi:10.1029/2002JB001782.

Beeler, N. M., and S. H. Hickman (2008), Direct measurement of asperity contact growth in quartz at hydrothermal conditions, *Eos Trans. AGU*, *89*(53), Fall Meet. Suppl., Abstract T52A-06.

Beeler, N. M., T. E. Tullis, A. K. Kronenberg, and L. A. Reinen (2007), The instantaneous rate dependence in low temperature laboratory rock friction and rock deformation experiments, *J. Geophys. Res.*, *112*, B07310, doi:10.1029/2005JB003772.

Boettcher, M. S., J. G. Hirth, and B. Evans (2007), Olivine friction at the base of oceanic seismogenic zones, *J. Geophys. Res.*, *112*, B0125, doi:10.1029/2006JB004301.

Boettcher, M. S., A. McGarr, and M. Johnston (2009), Extension of Gutenberg-Richter distribution to M_w −1.3, no lower limit in sight, *Geophys. Res. Lett.*, *36*, L10307, doi:10.1029/2009GL038080.

Brace, W. F., and J. D. Byerlee (1966), Stick slip as a mechanism for earthquakes, *Science*, *153*, 990–992.

Brantley, S. L., B. Evans, S. H. Hickman, and D. A. Crerar (1990), Healing of microcracks in quartz: Implications for fluid flow, *Geology*, *18*, 136–139.

Bruhn, R. L., W. T. Parry, W. A. Yonkee, and T. Thompson (1994), Fracturing and hydrothermal alteration in normal fault zones, *Pure Appl. Geophys.*, *142*, 609–645.

Burnham, C. W., J. R. Holloway, and N. F. Davis (1969), *Thermodynamic Properties of Water at 1000°C and 10 kb*, *Geol. Soc. Am. Spec. Pap.*, *132*, 96 pp., Geol. Soc. of Am., Boulder, Colo.

Chester, F. M. (1995), A rheologic model for wet crust applied to strike-slip faults, *J. Geophys. Res.*, *100*, 13,033–13,044, doi:10.1029/95JB00313.

Chester, F. M., and N. G. Higgs (1992), Multimechanism friction constitutive model for ultrafine quartz gouge at hypocentral conditions, *J. Geophys. Res.*, *97*, 1859–1870, doi:10.1029/91JB02349.

Chester, F. M., J. P. Evans, and R. L. Biegel (1993), Internal structure and weakening mechanisms of the San Andreas Fault, *J. Geophys. Res.*, *98*, 771–786, doi:10.1029/92JB01866.

Coblenz, W. S., J. M. Dynys, R. M. Cannon, and R. L. Coble (1980), Initial stage solid state sintering models, a critical analysis and assessment, in *Sintering Processes*, *Mater. Sci. Res.*, vol. 13, edited by G. G. Kuczgnski, pp. 141–157, Plenum Press, New York.

Cochran, E. S., Y. G. Li, P. M. Shearer, S. Barbot, Y. Fialko, and J. E. Vidale (2009), Seismic and geodetic evidence for extensive, long-lived fault damage zones, *Geology*, *37*(4), 315–318.

Dieterich, J. H. (1972), Time-dependent friction in rocks, *J. Geophys. Res.*, *77*, 3690–3697, doi:10.1029/JB077i020p03690.

Dieterich, J. H. (1978), Time-dependent friction and the mechanics of stick slip, *Pure Appl. Geophys.*, *116*, 790–806.

Dieterich, J. H. (1979), Modeling of rock friction: 1. Experimental results and constitutive equations, *J. Geophys. Res.*, *84*, 2161–2168.

Dieterich, J. H., and G. Conrad (1984), Effect of humidity on time- and velocity-dependent friction in rocks, *J. Geophys. Res.*, *89*, 4196–4202, doi:10.1029/JB089iB06p04196.

Dieterich, J. H., and B. D. Kilgore (1994), Direct observation of frictional contacts: New insights for sliding memory effects, *Pure Appl. Geophys.*, *143*, 283–302.

Dieterich, J. H., and B. D. Kilgore (1996), Imaging surface contacts: Power law contact distributions and contact stresses in quartz, calcite, glass, and acrylic plastic, *Tectonophysics*, *256*, 219–239.

Ellsworth, W. L., and K. Imanishi (2008), Near-source observations of earthquakes: Implications for earthquake rupture and fault mechanics, *Eos Trans. AGU, 89*(53), Fall Meet. Suppl., Abstract T22A-03.

Ellsworth, W. L., and P. E. Malin (2011), Deep rock damage in the San Andreas Fault revealed by *P*- and *S*-type fault zone guided waves, *Spec. Publ. Geol. Soc. London*, *359*, 39–53.

Farver, J., and R. A. Yund (1999), Oxygen bulk diffusion measurements and TEM characterization of a natural ultramylonite: Implications for fluid transport in mica-bearing rocks, *J. Metamorph. Geol.*, *17*, 669–683.

Farver, J. R., and R. A. Yund (1991), Measurement of oxygen grain boundary diffusion in natural, fine-grained quartz aggregates, *Geochem. Cosmochem. Acta*, *55*, 1597–1607.

Fournier, R. O., and R. W. Potter (1982), An equation correlating the solubility of quartz in water from 25° to 900°C at pressures up to 10 kb, *Geochim. Cosmochim. Acta*, *46*, 1969–1073.

Goldsby, D. L., A. Rar, G. M. Pharr, and T. E. Tullis (2004), Nanoindentation creep of quartz, with implications for rate- and state-variable friction laws relevant to earthquake mechanics, *J. Mater. Res.*, *19*, 357–365.

Gratier, J. P. (1993), Experimental pressure solution of halite by an indenter technique, *Geophys. Res. Lett.*, *20*, 1647–1650, doi:10.1029/93GL01398.

Hickman, S. H., and N. M. Beeler (1997), Direct measurements of diffusive contact growth in quartz at hydrothermal conditions, with implications for interseismic strength recovery, *Eos Trans. AGU*, *78*, F731, doi:10.1029/97EO00006.

Hickman, S. H., and N. M. Beeler (1999), The effect of grain boundary structure on the rate of quartz pressure solution, *Eos Trans. AGU*, *80*, F1028.

Hickman, S. H., and B. Evans (1987), Influence of geometry upon crack healing rate in calcite, *Phys. Chem. Miner.*, *15*, 91–102.

Hickman, S. H., and B. Evans (1992), Growth of grain contacts in halite by solution transfer: Implications for diagenesis, lithification, and strength recovery, in *Fault Mechanics and Transport Properties of Rocks*, edited by B. Evans and T.-F. Wong, pp. 253–280, Academic Press, San Diego, Calif.

Hickman, S., and B. Evans (1995), Kinetics of pressure solution at halite-silica interfaces and intergranular clay films, *J. Geophys. Res.*, *100*, 13,113–13,132, doi:10.1029/95JB00911.

Ildefonse, J.-P., and V. Gabis (1976), Experimental study of silica diffusion during metasomatic reactions in the presence of water at 550°C and 1000 bars, *Geochim. Cosmochim. Acta*, *40*, 297–303.

Johnson, K. (1985), *Contact Mechanics*, 452 pp., Cambridge Univ. Press, New York.

Johnston, M. J. S., R. D. Borcherdt, A. T. Linde, and M. T. Gladwin (2006), Continuous borehole strain and pore pressure in the near field of the 28 September 2004 *M* 6.0 Parkfield, California, earthquake: Implications for nucleation, fault response, earthquake prediction, and tremor, *Bull. Seismol. Soc. Am.*, *96*, s56–s72.

Li, Y. G., and P. E. Malin (2008), San Andreas Fault damage at SAFOD viewed with fault-guided waves, *Geophys. Res. Lett.*, *35*, L08304, doi:10.1029/2007GL032924-2008.

Li, Y.-G., and J. E. Vidale (2001), Healing of the shallow fault zone from 1994 to 1998 after the 1992 *M* 7.5 Landers California earthquake, *Geophys. Res. Lett.*, *28*, 2999–3002, doi:10.1029/2001GL012922.

Li, Y.-G., J. E. Vidale, K. Aki, and T. Burdette (1998), Evidence of shallow fault restrengthening after the 1992 *M* 7.5 Landers, California earthquake, *Science*, *279*, 217–219.

Li, Y.-G., P. Chen, E. S. Cochran, J. E. Vidale, and T. Burdette (2006), Seismic evidence for rock damage and healing on the San Andreas Fault, *Bull. Seismol. Soc. Am.*, *96*, 349–363.

Nakatani, M. (2001), Conceptual and physical clarification of rate and state friction: Frictional sliding as a thermally activated rheology, *J. Geophys. Res.*, *106*, 13,347–13,380, doi:10.1029/2000JB900453.

Nakatani, M., and C. H. Scholz (2004), Frictional healing of quartz gouge under hydrothermal conditions: 2. Quantitative interpretation with a physical model, *J. Geophys. Res.*, *109*, B07202, doi:10.1029/2003JB002938.

Nakatani, M., and C. H. Scholz (2006), Intrinsic and apparent short-time limits for fault healing: Theory observations and implications for velocity dependent friction, *J. Geophys. Res.*, *111*, B12208, doi:10.1029/2005JB004096.

Parry, W. T., and R. L. Bruhn (1990), Fluid pressure transients on seismogenic normal faults, *Tectonophysics*, *179*, 335–344.

Paterson, M. S., and T.-F. Wong (2005), *Experimental Rock Deformation: The Brittle Field*, 2nd ed., 348 pp., Springer, New York.

Rimstidt, J. D., and H. L. Barnes (1980), The kinetics of silica-water reactions, *Geochim. Cosmochim. Acta*, *44*, 1683–1699.

Rossi, B. (1965), *Optics*, 510 pp., Addison-Wesley, Redding, Mass.

Rutter, E. H. (1976), The kinetics of rock deformation by pressure solution, *Philos. Trans. R. Soc., A*, *283*, 203–219, doi:10.1098/rsta.1976.0079.

Scholz, C. H., and J. T. Engelder (1976), The role of asperity indentation and ploughing in rock friction: I. Asperity creep and stick-slip, *Int. J. Rock Mech. Min. Sci. Geomech. Abstr.*, *13*, 149–154.

Sleep, N. H., and M. L. Blanpied (1992), Creep, compaction and the weak rheology of major faults, *Nature*, *359*, 687–692.

Spiers, C. J., S. DeMeer, A. R. Nimeijer, and X. Zhang (2004), The kinetics of rock deformation by pressure solution and the role of thin aqueous films, in *Physicochemistry of Water in Geological and Biological Systems*, *Front. Sci. Ser.*, edited by S. Nakashima et al., pp. 129–158, Universal Academy Press, Tokyo.

Tullis, T. E., and J. D. Weeks (1987), Micromechanics of frictional resistance of calcite, *Eos Trans. AGU*, *68*, 405.

Wu, J., J. Hole, and J. Snoke (2010), Fault-zone structure at depth from differential dispersion of seismic guided waves: Evidence for a deep waveguide on the San Andreas Fault, *Geophys. J. Int.*, *182*, 343–354.